Journal of Aerosol Science 88 (2015) 48–57

Contents lists available at ScienceDirect

Journal of Aerosol Science

journal homepage: www.elsevier.com/locate/jaerosci

Ultrafine and nanoparticle formation and emission mechanisms during laser processing of ceramic materials

A.S. Fonseca [a,b,*], M. Viana [a], X. Querol [a], N. Moreno [a], I. de Francisco [c], C. Estepa [c], G.F. de la Fuente [c]

[a] Institute of Environmental Assessment and Water Research (IDÆA-CSIC), C/Jordi Girona 18, 08034 Barcelona, Spain
[b] Universidad de Barcelona, Facultad de Química, Martí i Franquès 1-11, 08028 Barcelona, Spain
[c] Instituto de Ciencia de Materiales de Aragón (ICMA – Universidad de Zaragoza), María de Luna 3, E-50018 Zaragoza, Spain

ARTICLE INFO

Article history:
Received 25 February 2015
Received in revised form
25 May 2015
Accepted 27 May 2015
Available online 6 June 2015

Keywords:
Tile sintering
Furnace
New particle formation
LDSA
Particle transport
Indoor air

ABSTRACT

The use of laser technology in the ceramic industry is undergoing an increasing trend, as it improves surface properties. The present work aimed to assess ultrafine and nanoparticle emissions from two different types of laser treatments (tile sintering and ablation) applied to two types of tiles. New particle formation mechanisms were identified, as well as primary nanoparticle emissions, with concentrations reaching up to 6.7×10^6 particles cm^{-3} and a mean diameter of 18 nm. Nanoparticle emission patterns were strongly dependent on temperature and raw tile chemical composition. Nucleation events were detected during the thermal treatment independently of the laser application. TEM images evidenced spherical ultrafine particles, originating from the tile melting processes. When transported across the indoor environment, particles increased in size (up to 38 nm) with concentrations remaining high (2.3×10^6 particles cm^{-3}). Concentrations of metals such as Zn, Pb, Cu, Cr, As and Tl were found in particles < 250 nm.

1. Introduction

Laser irradiation of ceramic material is a novel technique with numerous advantages regarding the sintering process such as speed, temperature and enhanced durability and surface properties of structural materials (Schmatjko, Endres, Schmidt, & Banz, 1988; Toenshoff & Gedrat, 1991; Jervis, Nastasi, Hubbard, & Hirvonen, 1993; de Francisco et al., 2011; Lahoz, de la Fuente, Pedra, & Carda, 2011). The use of high powered CO_2 lasers for industrial ceramic materials processing was studied in the framework of LIFE projects and is currently being assessed for two different industrial processes: (i) tile sintering in a high-temperature furnace and, (ii) ablation of ceramic materials. A recently developed "in-situ" melting method (tile sintering) makes use of a CO_2 laser scanner combined with simultaneous external heating of the substrate (in a conventional furnace) and uniform movement (Estepa & de la Fuente, 2006; de Francisco et al., 2011). This innovative technology allows to obtain coatings of practically any oxide material on an alumina substrate (Estepa & de la Fuente, 2006; de Francisco et al., 2011). In addition, this novel tool can also make use of CO_2 lasers in pulsed mode (induced laser ablation) to perform engravings on the surface of ceramics (Lahoz et al., 2011).

* Corresponding author at: Institute of Environmental Assessment and Water Research (IDÆA-CSIC), C/Jordi Girona 18, 08034 Barcelona, Spain. Tel.: +34 934006100; fax: +34 932045904.
E-mail address: ana.godinho@idaea.csic.es (A.S. Fonseca).

http://dx.doi.org/10.1016/j.jaerosci.2015.05.013

The high-energy nature of these laser processes implies a significant potential for the generation and emission of particles in the ultrafine and nanoparticle size range. However, nanoparticle emissions have so far never been evaluated for these industrial processes, mainly due to the novelty of this technology. The high temperatures applied in the furnace (up to 1195 °C) may cause chemical transformations in the raw tiles and the emission of particulate and/or gaseous pollutants into indoor air, which could be enhanced by the addition of the laser treatment.

Nanoparticle emissions from industrial processes are receiving increasing attention in the literature in recent years (Demou, Peter, & Hellweg, 2008; Pfefferkorn et al., 2010; Curwin & Bertke, 2011; Gandra, Miranda, Vilaça, Velhinho, & Teixeira, 2011; Koivisto et al., 2012; Van Broekhuizen, 2012; Gómez, Irusta, Balas, & Santamaria, 2013; Fonseca et al., 2014; Gomez et al., 2014; Voliotis et al., 2014; Koivisto et al., 2014). These works focus on different types of processes, and reveal that nanoparticle emissions and subsequent exposures may reach up to particle number concentrations of 1×10^6 parts cm^{-3} such as the cases of firing processes where the painting and glazing of ceramics occur (Voliotis et al., 2014), as well as during and welding/soldering (Gómez et al., 2013). However, because of the vast number of industrial processes with potential for nanoparticle emissions, the assessment of nanoparticle emissions under real-world scenarios should be encouraged. The present work addresses the emissions from a highly innovative process with a large potential for global-scale implementation in the ceramic industry, which has so far not been evaluated regarding nanoparticle emissions.

This work aimed to identify and characterize nanoparticle formation and emission mechanisms during tile sintering and laser ablation processes in a pilot plant-scale furnace (3 m long). Special attention was paid to new particle formation processes and their dependence on process variables such as temperature or raw tile chemical composition. Finally, nanoparticle transformations through transport in indoor air are also described.

2. Materials and methods

2.1. Materials and experimental procedure

Nanoparticle monitoring and sampling was conducted over three consecutive days (from 23rd October to 25th October 2013), in a research laboratory at the Instituto de Ciencia de Materiales de Aragón (ICMA) located in Zaragoza, Spain. The experiments were not extended over a longer period of time due to two main reasons: (a) particle emissions detected (see next section) were significantly above background concentrations, and thus the data obtained were considered statistically representative of the processes under study, and (b) the availability of the pilot-plant scale furnace was limited. The laser used included a Rofin-Sinar 350 W SLAB-type CO_2 laser resonator and an optical beam steering system (Estepa & de la Fuente, 2006). Two types of laser-based processes were assessed:

a) *Tile sintering*
Industrial ceramic tiles were sintered by laser irradiation in a high-temperature furnace. The tile sintering process was performed using a CO_2 laser emitting at a wavelength $\lambda = 10.6$ μm. The tiles were introduced in the furnace at a constant speed (1.5 m h^{-1}) in an orthogonal direction to the laser focus. The samples were gradually externally heated with a resistance furnace in a temperature range from ambient temperature up to 850 °C. Afterwards, the tiles followed the standard thermal cycles used at industrial-scale, with gradually increasing temperatures which reached peak values of about 1195 °C and 1115 °C for porcelain and red clay tiles, respectively.
Six conventional industrial tiles were selected: raw porcelain (#1), porcelain with frit (#2), porcelain with frit and colored decoration (#3), raw red clay (#4), red clay with frit (#5) and red clay with frit and colored decoration (#6). These are six of the most frequently used types of tiles in the industry.

b) *Laser ablation*
Laser ablation is the process by which material is expelled from a surface by irradiating it with a pulsed laser (Bäuerle, 1996; Rubahn, 1999; Lahoz et al., 2011). Fig. S1 in the supplementary information presents an illustration of these effects. It illustrates the presence of a melted layer at the surface of the porcelain tiles where the laser is irradiating. Particle emissions during laser ablation were only assessed for one type of material (raw porcelain; #7).

2.2. Sampling locations

The laboratory under study had a surface of 29 m^2. The particle monitors and samplers were placed simultaneously at the emission source, directly above the furnace, at a second location indoors to assess the influence of transport (referred to as the breathing zone), and in outdoor air. Measurements at the emission source were performed between the furnace and the extraction system, and were therefore only influenced by emissions generated in the furnace (no contamination from background air was possible). Fig. S2 of the supplementary information shows the layout of the indoor area under study and sampling locations.

The height of the furnace from the floor is 1.1 m. At the source, instrument inlets were placed inside a 15 cm diameter tube (2.05 m above ground level), which acted as ventilation system for the furnace. In addition, measurements were made in the worker area, located at approximately 2 m from the furnace. Inlets were placed at breathing zone height (~1.6 m).

2.3. Real time measurements

Particle measurements in the range 5 nm to 20 μm were performed using different instrumentation, aiming to combine the specific advantages of each of the instruments used with the purpose of overcoming their specific limitations, especially regarding lower particle sizes and maximum particle number concentrations measured:

a) *At the emission source:*
- An electrical mobility spectrometer (NanoScan, SMPS TSI Model 3910; sample flow rate 0.7 L min^{-1}) to measure the particle mobility size distribution in 13 channels from 10 to 420 nm mobility diameter. Time resolution was 1 min.
- An Optical Particle Sizer (OPS, TSI Model 3330; sample flow rate 1 L min^{-1}) which measures the optical size distribution from 0.3 to 10 μm in 16 channels with 1 min time resolution.
- A water-based condensation particle counter (WCPC, TSI Model 3785; sample flow rate 1 L min^{-1}) measuring total particle number concentration between 5 nm and 3 μm with 1 min time resolution.

b) *In the breathing zone:*
- An optical particle counter (OPC; Grimm Model 1.108) to measure particle mass in the range 0.3–20 μm. The sample flow rate and the sampling time interval were 1.2 L min^{-1} and 1 min, respectively. The particles were classified in 15 channels according to their optical diameter.

In addition, the following instruments were placed simultaneously at the emission source and at the breathing zone:
- Two light-scattering laser photometers (DustTrak™ DRX aerosol monitor TSI Model 8533; sample flow rate 3.0 L min^{-1}) to measure PM_{10}, $PM_{2.5}$, PM_1 with 1 min time resolution. The PM values in the breathing zone were corrected with respect to reference gravimetric values, using a high-volume reference sampler. This was not possible, however, for the instrument at the emission source, and therefore only uncorrected values are reported.
- Two miniature diffusion size classifiers DiscMini Matter Aerosol (Fierz, Houle, Steigmeier, & Burtscher, 2011) to measure total particle number, mean particle diameter and alveolar lung deposited surface area (LDSA) concentration. The sample flow rate and the sampling time interval were 1 L min^{-1} and 1 min, respectively. The instrument detects particles with a mode diameter between 10 and 300 nm.

Because certain of these instruments monitored similar parameters (e.g. WCPC and NanoScan monitoring particle number concentrations although in different size ranges), in the results and discussion section only one of the datasets will be discussed for each parameter. In the case of total particle number (N), the results presented will be those obtained with the WCPC, unless otherwise specified, because of the highest concentration range measurable with this instrument (up to 10^7 parts cm^{-3}, as opposed to 10^6 parts cm^{-3} with NanoScan or DiscMini). The same applies for mean particle diameter, which will be discussed using the DiscMini data, because it is the only instrument for which particle diameter data were available simultaneously in the emission source and breathing zone. In the original setup, the use of different instruments measuring similar parameters aimed to maximize the number of valid data points obtained, given that the risk of exceeding the measurement capabilities of the instruments was high (due to the high nanoparticle emissions expected). Intercomparisons carried out during data processing (not shown) evidenced a high degree of comparability ($\pm$ 15% of relative difference) between the different instruments for those with matching particle size ranges.

2.4. Sample collection

Particles emitted at the source were collected on 25 mm polycarbonate filters (one sample per ceramic material, plus one sample each night) with 0.8 μm pore size. Samples were collected using cassettes (SKC Inc., inlet diameter 1/8 in.) connected to SKC Leland Legacy pumps operating at 0.21 m^3 h^{-1} (3.5 L min^{-1}). The sampling periods ranged from 20 min to 102 min, which correspond to air volumes sampled between 0.07 m^3 and 0.36 m^3, respectively.

In addition, one accumulated sample was collected over the entire sampling period (26 h) by means of Personal Cascade Impactor Sampler (SioutasTM PCIS, SKC Inc.) (Misra et al., 2002). Two PCIS were placed simultaneously indoor and outdoor connected to pumps operating at 9 L min^{-1}. The collection substrates were 37 mm quartz fiber filters for the < 0.25 μm (Pall) stage and 25 mm teflon-PTFE filters for the 0.25–2.5 μm and 2.5–10 μm stages (Pall).

Mass concentrations were gravimetrically determined by pre- and post-weighting the filters on a microbalance.

Particle morphology, chemical composition, and size were analyzed by transmission electron microscopy (TEM, Jeol, JEM 1220, Tokyo, Japan), coupled with an energy-dispersive X-ray (EDX) spectroscopy. Particles for TEM were collected onto Quantifoil® gold (Au) grids with 1 μm diameter holes – 4 μm separation of 200-mesh at the emission source. TEM grids were attached to air sample cassettes (SKC Inc., USA, inlet diameter 1/8 in. and filter diameter 25 mm) on polycarbonate membrane filters. Air flow was driven by pumps operating at 3.5 L min^{-1} and collection efficiency for particles was assumed to be 100%. TEM sampling durations and sampled air volume were the same as for the polycarbonate filter samples described above.

2.5. Sample treatment and analysis

All the filters and samples of each raw ceramic material were acid digested by using nitric acid (HNO_3), hydrofluoric acid (HF) and perchloric acid ($HClO_4$) following the method proposed by Querol et al. (2001) for the analysis of major and trace elements by means of ICP-AES (IRIS Advantage TJA Solutions, THERMO) and ICP–MS (X Series II, THERMO). Laboratory blank filters were analyzed following the same methodology. Element concentrations were blank corrected.

In order to identify the mineralogical phases, a portion of each raw studied ceramic material was analyzed by X-ray powder diffraction (XRD).

3. Results and discussion

3.1. Chemical and mineral composition of the raw tiles

The chemical composition of the raw porcelain and red clay tiles is reported in Table S1 of the supplementary information. The composition of red clay and porcelain tiles was clearly distinct. Porcelain was characterized by higher concentrations of SiO_2, Al_2O_3, Na_2O and P_2O_5 with the largest difference being observed for Na_2O (93% higher than in red clay tiles). The relative concentrations of the remaining metal oxides were always higher for red clay tiles. The relative concentrations of trace elements were also higher in red clay tiles, which are enriched in all the elements analyzed, except for Y and Nb.

Fig. S3 of the supplementary information shows the diffraction pattern determined by XRD analysis for each type of tile. Common crystalline constituents found in both types of tiles were quartz, SiO_2 (00-046-1045); kaolinite, $Al_2Si_2O_5(OH)_4$ (00-014-0164); illite, $(K,H_3O)(Al_2Si_3AlO_{10}(OH)_2)$ (00-026-0911) and, anhydrite, $CaSO_4$ (00-037-1496). Conversely, mineral phases such as albite, $NaAlSi_3O_8$ (00-019-1184) were only found in porcelain tiles, whereas calcite, $CaCO_3$ (00-005-0586), dolomite, $CaMg(CO_3)_2$ (00-036-0426), hematite, Fe_2O_3 (00-033-0664) and microcline, $KAlSi_3O_8$ (00-019-0932) were only found in red clay tiles.

The composition of frit and pigments used for decoration may not be provided due to confidentiality reasons. Pigments are essentially composed of oxides of Al, Cu, Cr, Co, Mn, Fe, Pb, and Sn (Taylor, Bull, & Ceramics, 1986; Casasola, Rincón, & Romero, 2012; Celades, 2013). Furthermore, $ZrSiO_4$, ZrO_2, ZnO, TiO_2 and SnO_2 are frequently used as opacifying agents to produce opaque frits (Jacobs, 1954; Romero, Rincón, & Acosta, 2003; Lahoz et al., 2011; Casasola et al., 2012).

3.2. Nanoparticle emissions

The time series of particle number concentrations, measured at the emission source (the furnace for sintering processes, and outside the furnace for ablation process) are shown in Fig. 1. Table 1 summarizes the mean and maximum concentrations obtained in terms of number and mass concentrations, as well as the mean particle diameter for the emissions from each of the materials sintered (from #1 to #6), the material ablated (#7) and for background air (non-activity period).

Over the two-hour periods during which each of the tiles underwent the thermal treatment, major nanoparticles emissions were registered. On average, mean and maximum *N* minute concentrations were 1 and 2 orders of magnitude (respectively) higher than background levels, and by applying the methodology described by Asbach et al. (2012) and based on the ratio between workplace air concentrations and 3 times the standard deviation of the background concentration, it may be concluded that nanoparticle emissions during thermal treatment were statistically representative. Mean particle diameters were lower (8–18 nm) than in background air (38 nm). The fact that measurements were carried out in a pilot-plant scale furnace suggest that the emission processes detected are likely to take place also at industrial scale.

The highest nanoparticle emissions were registered during red clay tile sintering and, in particular for material #5, reaching a maximum of 6.7×10^6 parts cm^{-3} (particle mean diameter = 18 nm). Maximum nanoparticle emissions during sintering of a similarly coated material (#2) were lower by a factor of 2, thus suggesting that majority of the nanoparticles emissions originate from the base of the tiles, as opposed to the coating materials. On average, nanoparticle emissions were

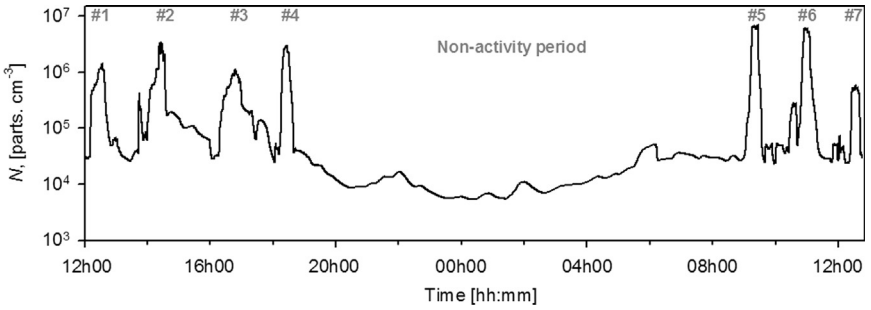

Fig. 1. Time series of particle number concentration measured at emission source.

Table 1
Average and maximum (in parenthesis) particle number concentrations, particle diameter and mass concentrations measured during tile sintering, ablation and background. Mean values corresponding to each sintering and ablation process, approximately 1.5 h and 20 min in duration, respectively. Maximum values are 1 min means.

Material	N [parts cm^{-3}]	D_p [nm]	PM_1 [μg m^{-3}]	$PM_{2.5}$ [μg m^{-3}]	PM_{10} [μg m^{-3}]
#1: Raw porcelain	2.7×10^5 (1.4×10^6)	8 (16)	5.4 (25.0)	6.5 (26.0)	10.2 (40)
#2: Porcelain with frit coated	5.7×10^5 (3.3×10^6)	11 (24)	6.0 (41.0)	7.0 (48.0)	12.4 (115.0)
#3: Porcelain with frit and decoration coated	3.6×10^5 (1.1×10^6)	11 (22)	22.6 (52.0)	23.5 (53.0)	28.5 (58.0)
#4: Raw red clay	4.2×10^5 (3.1×10^6)	16 (31)	10.2 (43.0)	11.3 (50.0)	16.9 (115.0)
#5: Red clay with frit coated	9.7×10^5 (6.7×10^6)	18 (30)	24.1 (125.0)	25.8 (128.0)	30.4 (131.0)
#6: red clay with frit and decoration coated	9.5×10^5 (6.1×10^6)	15 (25)	19.5 (64.0)	21.5 (66.0)	26.1 (69.0)
#7: Ablation	3.8×10^5 (5.8×10^5)	80 (130)	610 (1110)	650 (1200)	670 (1300)
Background[a]	1.6×10^4 (9.8×10^4)	38 (60)	2.8 (24.0)	3.4 (27.0)	4.7 (57.0)

[a] Corresponding to non-activity period.

higher for red clay sintering (7.8×10^5 parts cm^{-3}) when compared to porcelain (4.0×10^5 parts cm^{-3}). This is an especially relevant finding for the tile industry, given that red clay materials are usually preferred because of their lower cost with respect to porcelain. However, due to esthetic reasons, the demand for porcelain tiles is currently increasing in the global ceramic market. Regarding mean particle diameter, emissions from red clay sintering were on average coarser (16 nm) than from porcelain tiles (10 nm), even if both particle diameters are extremely small especially in comparison to background air.

A relatively similar pattern was observed for particle mass. The highest total PM emissions were generated during sintering of frit coated red clay tiles (#5; 32.8 μg m^{-3}), although followed closely by frit and decoration coated porcelain (#3; 30.5 μg m^{-3}). The lowest emissions in terms of mass originated from porcelain sintering where a reduce influence on the formation of larger particles were found, especially for coated porcelain.

Fig. 1 and Table 1 also show the results from the ablation (#7). Results show that ablation emissions were highest in terms of mass for all size ranges and materials and lowest in terms of particle number concentration (3.8×10^5 parts cm^{-3}) (with exception of material #1, and #3). Furthermore, the particle size was highest showing a mean diameter of 80 nm. These observations were expected during ablation because it is a mechanical process (as opposed to a thermal process). The TEM samples show a large number of spherical morphology particles below 1 μm in indoor air (Fig. 2), especially during the ablation process (d) where aggregates of particles in the nano-size range are observed. This is expected to occur due to the fact that laser engraving induces phase transitions, causing break down of the original material (Lahoz et al., 2011). During ablation, particles are produced with a more spherical shape whereas during sintering (Fig. 2a–c) they are finer and may be interpreted as portions of melted material involved in melting processes at a high temperature under the laser beam. Chemical analysis by EDX showed that the nanoparticles are mostly constituted by elements such as Zn, Cu and Fe due to the extensive use of these substances as opacity and pigmentation agents in ceramic tiles (Casasola et al., 2012; Celades, 2013).

3.3. Particle size distributions

The particle number distributions corresponding to porcelain and red clay sintering are shown in Fig. 3a and b, respectively. Additionally, results from raw porcelain ablation are presented in Fig. 3a. The mean particle diameters produced from sintering were below mostly 35 nm (for $>80\%$ of the particles). Conversely, the ablation process produced mainly particles between 65 and 200 nm (for $>90\%$ of the particles) in number.

The size distributions present different trends during sintering and ablation. During sintering, trimodal shaped distributions were measured, with mode values at 10–20 nm, 20–85 nm and 85–420 nm. This was observed for red clay and porcelain tiles. Conversely, laser ablation of porcelain tiles produced a bimodal curve, with mode values 10–50 nm and 50–420 nm, with a clear prevalence of coarser particles (>100 nm) as expected.

Particle size distribution seemed to depend on the type of material. In particular, for particles ranging between 10 and 85 nm, mean particle number concentrations from porcelain tiles were higher (4.1×10^5 parts cm^{-3}) than from red clays (3.0×10^5 parts cm^{-3}). However, the number concentration for particles below 11.5 nm during sintering of material #6 were higher than for material #3, respectively. Concerning particles between 85 and 420 nm in diameter, particle number concentrations were higher for red clays (3.7×10^4 parts cm^{-3}) than for porcelain tiles (1.9×10^4 parts cm^{-3}).

3.4. Particle formation and emission mechanisms

Fig. 4 shows an example of time series of particle number concentrations and size for the particles emitted during the entire thermal cycle for porcelain and red clay tiles with frit coating (materials #2 and #5). Table 2 summarizes, for all of the materials, the mean and geometric standard deviation (σ) of particle number concentrations (N) and particle diameter (D_p).

Two different emission behaviors, strongly linked to temperature, were registered. In the first 30 min, when porcelain and red clay tiles were externally heated in the furnace in a temperature range between 850–1195 °C and 850–1115 °C for porcelain and red clay tiles respectively, a thermally-induced emission pattern was observed starting from 1.3×10^5 parts for

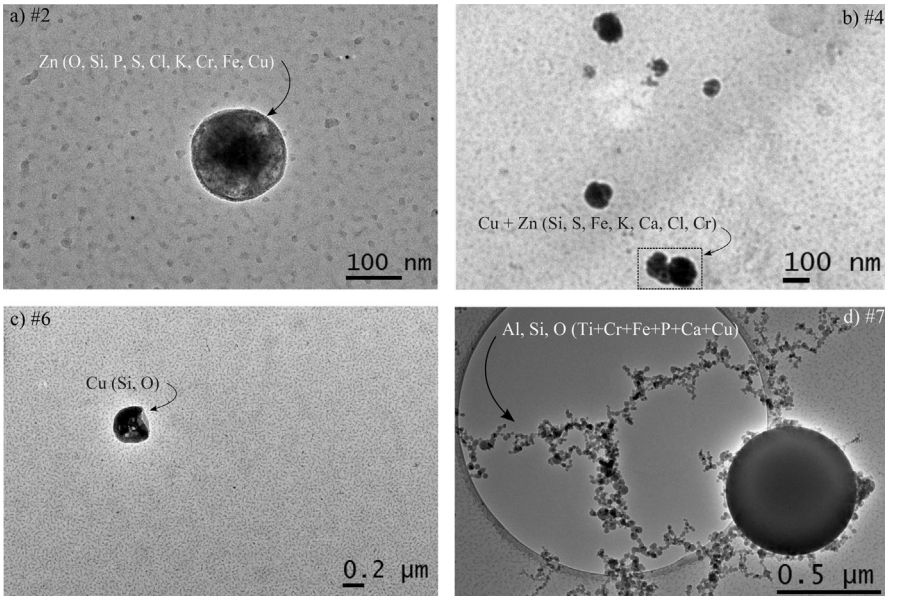

Fig. 2. TEM images of nanoparticles collected in indoor air during: (a) sintering of porcelain with frit coated; (b) sintering of raw red clay; (c) sintering of red clay with frit and decoration coated; (d) ablation of raw porcelain. Corresponding identified particles by EDX are shown in each figure.

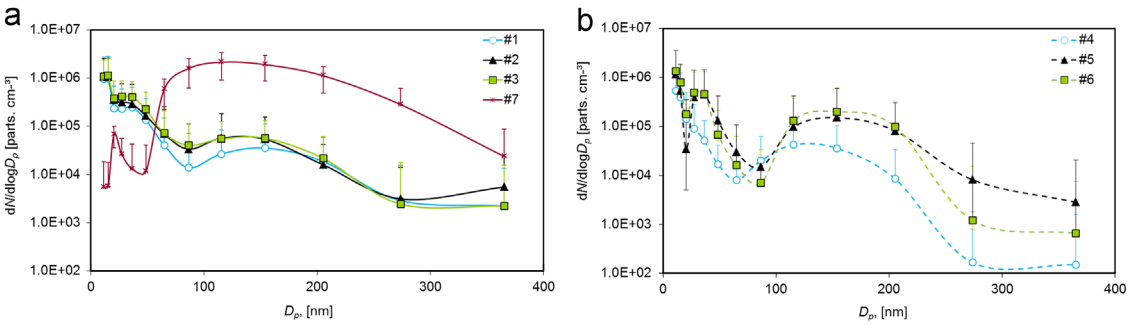

Fig. 3. Size distributions of particles including standard error bars during porcelain and red clay sintering and porcelain ablation. Error bars represent ± standard deviation (σ).

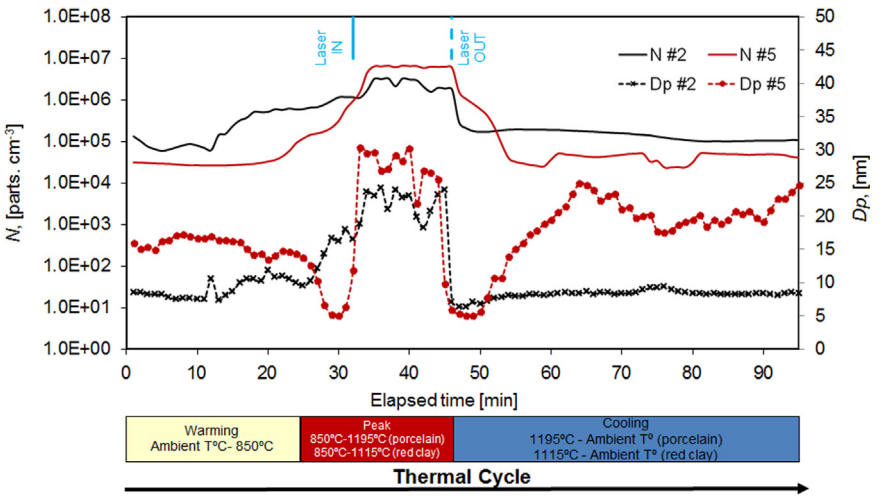

Fig. 4. Time series of particle number concentrations (solid lines) and mean particle size (dashed lines with bullets) during sintering of porcelain and red clay with frit coated.

Table 2
Geometric mean and standard deviation (in parenthesis) of particle number concentrations and particle diameter, only during the period of laser incidence.

Material	N [parts cm^{-3}]	D_p [nm]
#1: Raw porcelain	7.4×10^5 (5.0×10^5)	8 (2)
#2: Porcelain with frit coated	2.5×10^6 (7.0×10^5)	21 (5)
#3: Porcelain with frit and decoration coated	8.5×10^5 (1.6×10^5)	15 (4)
#4: Raw red clay	2.3×10^6 (7.0×10^5)	24 (5)
#5: Red clay with frit coated	5.6×10^6 (1.8×10^6)	24 (8)
#6: red clay with frit and decoration coated	5.0×10^6 (1.4×10^6)	15 (4)

Table 3
Average and maximum (in parenthesis) particle number concentrations, mean particle diameter and mean LDSA measured at breathing zone during tile sintering and background concentrations.

Material	N [parts cm^{-3}]	D_p [nm]	PM_1 [μg m^{-3}]	$PM_{2.5}$ [μg m^{-3}]	PM_{10} [μg m^{-3}]	LDSA [μm^2 cm^{-3}]
#1: Raw porcelain	3.0×10^5 (1.2×10^6)	18 (26)	6.1 (8.9)	7.3(12.0)	13.2 (19.9)	277 (1547)
#2: Porcelain with frit coated	5.6×10^5 (1.4×10^6)	13 (28)	5.9 (7.8)	7.0(10.4)	12.5 (21.4)	371 (1686)
#3: Porcelain with frit and decoration coated	8.0×10^5 (2.3×10^6)	16 (29)	8.2 (12.8)	10.7(18.3)	17.0 (26.2)	687 (2271)
#4: Raw red clay	7.5×10^4 (4.7×10^5)	27 (36)	6.5 (8.0)	8.0(10.5)	13.8 (16.7)	69 (223)
#5: Red clay with frit coated	1.1×10^5 (3.1×10^5)	26 (38)	7.3 (9.1)	9.3(12.4)	15.7 (19.4)	115 (229)
#6: red clay with frit and decoration coated	2.7×10^5 (1.2×10^6)	19 (35)	7.7 (13.8)	10.0(20.2)	16.3 (28.5)	213 (551)
Background[a]	2.6×10^4 (1.7×10^5)	36 (58)	5.6 (12.9)	6.4(18.9)	11.4 (30.9)	35 (118)

[a] Corresponding to non-activity period min means.

porcelain cm^{-3} and 3.1×10^4 parts cm^{-3} for red clay tiles frit coated. For material #2, the increase in mean particle size also followed the increase of the temperature in the furnace increasing from 9 nm probably due to condensation of pre-existing nanoparticles after emission. The evolution of the particle size of material #5 exhibited a different pattern: for the first 20 min, particle number concentrations and size remained stable and during the following 10 min, particle number concentration started to increase and a decrease in particle size was detected reaching lowest values of 5 nm. This suggests the occurrence of new particle formation processes by nucleation (nanoparticles < 30 nm in diameter being formed; Kumar, Fennell, & Britter, 2008), which would result in higher particle number concentrations with a lower particle size. This was probably due to the S-bearing species in the raw material such as anhydrite ($CaSO_4$), which decomposes at high temperatures (Chinchón, Querol, Fernández-Turiel, & López-Soler, 1991), into CaO and SO_2. In the furnace, SO_2 probably causes nucleation events induced by H_2SO_4 as exhaust gases cool down (Kulmala et al., 2004). These events were not detected so clearly with porcelain materials, probably due to their much lower SO_4^{2-} content (0.03%).

Upon introduction of the laser beam (within the peak temperature zone, Fig. 4), the particle number concentrations increased reaching maximum values of 3.3×10^6 parts cm^{-3} (porcelain) and 6.7×10^6 parts cm^{-3} (red clay) with mean diameters of 24 nm and 30 nm, respectively. The increase in both particle size and concentration probably resulted from additional emissions of primary nanoparticles of melted products from the surface materials due to the laser treatment with slightly coarser particle diameters (> 24 nm as opposed to < 20 nm during the thermal treatment). The presence of submicron spherical nanoparticles (most < 100 nm) resulting from melting was confirmed by TEM images (Fig. 2).

Upon completion of the laser treatment (minute 46, Fig. 4), nucleation events were once again detected as a decrease in mean particle size to 5–6 nm. On minute 50 (cooling zone), particle number concentrations for porcelain tiles dropped back to the registered levels in the beginning of the sintering process (1×10^5 parts cm^{-3}). Concerning the red clay tiles, the decrease in particle number concentration to background levels (3×10^4 parts cm^{-3}) occurred slightly later, on minute 55. Finally, whereas a constant of particle number concentration was detected, significant particle growth was observed for red clay tiles during the cooling stage, probably due to condensation of gaseous species and/or the agglomeration of existing finer nanoparticles from nucleation. This particle growth was not observed for porcelain probably due to the less intense particle nucleation rates observed for these materials.

Similar patterns were obtained for all the materials analysed, although with the highest nanoparticle emissions during laser treatment being registered for material #5, followed by material #6, reaching an average of 5.6×10^6 parts cm^{-3} and 5.0×10^6 parts cm^{-3}, respectively. Nanoparticle emissions during laser treatment on similarly coated porcelain materials, such as #2 and #3, were lower than coated red clay tiles by a factor of 2.2 and 5.9, respectively. Although for porcelain and red clay the size of the emitted particles exhibited diameters finer than 24 nm, the particles emitted by porcelain sintering under laser treatment were finer than for red clay. Conversely, particle number concentrations emitted were higher from red clay than from porcelain. These results have direct implications for the ceramic industry, given the current increasing

global demand for porcelain tiles and the similarly decreasing demand for red clay tiles. This would imply increasing exposures to nanoparticles of lower diameters (<20 nm) in ceramic industrial plants.

3.5. Transport of emissions across indoor air

Table 3 shows the results obtained at the secondary indoor location (the worker breathing zone) during tile sintering. The patterns observed in the breathing zone were somewhat different to those from the emission source.

Particle concentrations decreased from the furnace to the breathing zone for four of the six materials studied. The exceptions were material #1 and material #3. These decreases were interpreted as resulting from dilution of emission with workplace air, and also from coagulation and agglomeration of the particles emitted at the furnace. On average, mean and maximum N minute concentrations in the breathing zone were one order of magnitude higher than background levels for all the materials. Mean particle diameters in the breathing zone were 13–27 nm, larger than in the furnace but smaller than background air (36 nm). This increase in particle diameter with regard to the furnace area is consistent with particle ageing and coagulation particle processes described above.

In contrast to the emissions monitored at the emission source, the highest nanoparticle concentrations in the breathing zone were registered during material #3 with a maximum of 2.3×10^6 parts cm^{-3} (particle mean diameter=16 nm). On average, nanoparticle concentrations were lower for red clay sintering (1.5×10^5 parts cm^{-3}) when compared to porcelain (5.5×10^5 parts cm^{-3}). Similarly to the mean particle diameter measured at the furnace, particles from red clay sintering were on average coarser (24 nm) than from porcelain tiles (16 nm). Once they reached the breathing zone, particles from porcelain and red clays were 1.6 and 1.5 times coarser than the same particles at the emission source, respectively.

In terms of mass, a relatively similar pattern to the one described for the furnace area, was registered. Increases in particle mass were detected after transport to the breathing zone.

The alveolar LDSA of the nanoparticles emitted during tile sintering and measured in the breathing zone was significantly larger than in background air. Background air LDSA concentrations were 35 $\mu m^2\ cm^{-3}$ and they increased by a factor of 2–20 in the breathing zone. LDSA concentrations were higher during porcelain sintering than during red clay sintering. In terms of average values, sintering of frit coated porcelain tile exhibited the highest mean value ($6.9\times10^2\ \mu m^2\ cm^{-3}$). Finally, alveolar LDSA concentrations during tile ablation exceeded the levels recorded during sintering, reaching an average value of $6.3\times10^3\ \mu m^2\ cm^{-3}$ (data not shown). Monitored levels of LDSA in both processes were significantly higher than the outdoor levels registered in major European cities such as Dusseldorf, Germany (30–45 $\mu m^2\ cm^{-3}$) (Kuhlbusch et al., 2004), Lisbon, Portugal (35–89 $\mu m^2\ cm^{-3}$) (Albuquerque, Gomes, & Bordado, 2012; Gomes, Bordado, & Albuquerque, 2012) and Barcelona, Spain ($37\pm26\ \mu m^2\ cm^{-3}$) (Reche et al., 2015).

3.6. Particle chemical characterization

The chemical composition of particles collected in indoor and outdoor air for 26 h is summarized in Tables S2 (major species) and S3 (trace elements) of the supplementary information.

Indoor mass concentrations of $PM_{<0.25}$, $PM_{0.25-2.5}$, and $PM_{2.5-10}$ were 43.1 $\mu g\ m^{-3}$, 5.3 $\mu g\ m^{-3}$ and 4.8 $\mu g\ m^{-3}$ respectively. $PM_{<0.25}$ mass concentrations were higher than in other size fractions for most of the elements analysed in indoor air, evidencing the influence of sintering emissions in the lowest particle size range. The main indoor components of $PM_{<0.25}$ were SiO_2 (2.0 $\mu g\ m^{-3}$), K_2O (3.7 $\mu g\ m^{-3}$), SO_4^{2-} (4.6 $\mu g\ m^{-3}$), Zn (0.8 $\mu g\ m^{-3}$), Cr (0.6 $\mu g\ m^{-3}$), Pb (0.1 $\mu g\ m^{-3}$) and As (0.05 $\mu g\ m^{-3}$). Indoor $PM_{2.5-10,}$ was enriched in Zr (12.2 $ng\ m^{-3}$) and Sr (4.3 $ng\ m^{-3}$), when compared with outdoor concentrations (Zr < detection limit and Sr=1.2 $ng\ m^{-3}$ of Sr), probably linked to frit and pigments used in the ceramic tiles (Querol et al., 2007; Minguillon et al., 2009; Sánchez de la Campa et al., 2010). This statement is in agreement with the chemical composition of the PM collected during each sintering and ablation process, which is displayed in Table S4 of the supplementary information.

Indoor/outdoor concentration ratios (I/O) (Fig. S4 in the supplementary information) were especially high for typical tracers of components in $PM_{<0.25}$ used in the mix of frits and pigments in tile decoration such as Cr, Mn, Ni, Cu, Ce and Pb (Minguillon et al., 2009; Sánchez de la Campa et al., 2010). Concerning $PM_{0.25-2.5}$, the main species with I/O ratios >1 were P_2O_5 and ZnO. Zn is very often used in frit and enamel formulas (Casasola et al., 2012; Celades, 2013). Finally, the coarse particles ($PM_{2.5-10}$) showed a larger occurrence of I/O > 1 for Ba. I/O < 1 indicate the predominance of outdoor sources or particle losses and evaporation processes indoors. This was the case for certain crustal elements of outdoor origin such as Al, Ti and Fe, indicating that their origin is mainly linked to traffic re-suspension of road dust (Querol et al., 2007). As expected, secondary inorganic aerosols such as SO_4^{2-} also showed ratios <1 in the accumulation mode (Seinfield & Pandis, 2012; Viana et al., 2014). The chemical profile of particles emitted from red clay sintering was characterized by high concentrations of mainly K, Rb, TI and probably Zn and SO_4^{2-}, Cu and Sn (Table S4). Inversely, emissions of CaO were found to be 1.2–3.2 times higher from porcelain tiles sintering than from red clay tile sintering.

4. Conclusions

Nanoparticle formation, emission mechanisms, and impact on exposure were assessed for different ceramic materials during tile sintering and laser ablation processes in a pilot plant scale furnace. Six conventional and the most frequently used types of tiles in the ceramic industry were assessed.

The main findings from this study may be summarized as follows:

- Nanoparticle emissions were detected in high concentrations (mean minute concentration up to 9.7×10^5 parts cm^{-3} over 1.5 h), with mean diameter of 18 nm.
- Two different emission behaviors were detected: (i) Thermally induced emission, and (ii) nanoparticle formation through nucleation. These behaviors were, independent of the laser treatment, and they were strongly linked to tile composition.
- It is concluded that temperature plays a major role in particle emission in this kind of industrial process.
- New particle formation processes by nucleation occurred mostly during red clay tile sintering and probably due to S-bearing species in the raw material (e.g., $CaSO_4$).
- Ablation emissions were highest in terms of mass for all size ranges and highest in terms of particle size (mean diameter of 80 nm).
- When emissions were transported across the indoor area, particle number, mass and LDSA concentration decreased but remained at extremely high levels (up to $N = 2.3 \times 10^6$ parts cm^{-3}; LDSA $= 2.3 \times 10^3$ μm^2 cm^{-3}) with small particle sizes (13–27 nm). Mean particle diameters in the breathing zone were larger than in the furnace (8–18 nm) but smaller than in background air (36 nm).
- The highest concentrations of metals (mainly Zn, Pb, Cu, Cr, As and Tl) were found in the ultrafine fraction < 0.25 μm.

It is recommended that preventive and protective actions (e.g., exhaust fume extraction) should be undertaken in ceramic industries using laser irradiation during tile sintering, but also during conventional thermal treatment.

Further research is underway in order to confirm the findings from this study and to provide a better understanding of nanoparticle formation mechanisms and of potential exposures in workplace air, in a larger number of representative samples and under pilot plant conditions.

Role of funding source

The funding sources had no involvement in study design, in the collection, analysis and interpretation of data, in the writing of the text, nor in the decision to submit the article for publication.

Acknowledgments

This study was supported by the European Community's Seventh Framework Program (FP7-PEOPLE-2012-ITN) under Grant no. 315760 (HEXACOMM Project) and by the National Project IMPACT (CGL2011-26574). Additional funding was provided by LIFE projects AIRUSE (LIFE11 ENV/ES/584), CERAMGLASS (LIFE11 ENV/ES/560) and LASERFIRING (LIFE09 ENV/ES/435). The authors also gratefully acknowledge the technical staff in Materials Science Institute of Aragón (ICMA), especially to Carlos Borrel and the colleagues Jesús Parga, Noemí Pérez and Andres Alastuey from IDÆA-CSIC for their support and collaboration.

Appendix A. Supplementary information

Supplementary data associated with this article can be found in the online version at http://dx.doi.org/10.1016/j.jaerosci.2015.05.013.

References

Albuquerque, P.C., Gomes, J.F., & Bordado, J.C. (2012). Assessment of exposure to airborne ultrafine particles in the urban environment of Lisbon, Portugal. *Journal of the Air & Waste Management Association*, *62*(4), 373–380.

Asbach, C., Kuhlbusch, T., Kaminski, H., Stahlmecke, B., Plitzko, S., Götz, U., et al. (2012). NanoGEM standard operation procedures for assessing exposure to nanomaterials, following a tiered approach.

Bäuerle, D. (1996). *Laser processing and chemistry*. Springer-Verlag: Berlin.

Casasola, R., Rincón, J.M., & Romero, M. (2012). Glass–ceramic glazes for ceramic tiles: A review. *Journal of Materials Science*, *47*(2), 553–582, http://dx.doi.org/10.1007/s10853-011-5981-y.

Celades, I. (2013). *Caracterización física, química, mineralógica y morfológica del material particulado emitido por focos canalizados de la industria de baldosas y fritas cerámicas [Ph.D.]*. Universitat Jaume I de Castellón: Castellón.

Chinchón, J.S., Querol, X., Fernández-Turiel, J.L., & López-Soler, A. (1991). Environmental impact of mineral transformations undergone during coal combustion. *Environmental Geology and Water Sciences*, *18*(1), 11–15, http://dx.doi.org/10.1007/bf01704573.

Curwin, B., & Bertke, S. (2011). Exposure characterization of metal oxide nanoparticles in the workplace. *Journal of Occupational and Environmental Hygiene*, *8*(10), 580–587.

de Francisco, I., Lennikov, V.V., Bea, J.A., Vegas, A., Carda, J.B., & de la Fuente, G.F. (2011). In-situ laser synthesis of rare earth aluminate coatings in the system Ln–Al–O (Ln = Y, Gd). *Solid State Sciences*, *13*(9), 1813–1819, http://dx.doi.org/10.1016/j.solidstatesciences.2011.07.013.

Demou, E., Peter, P., & Hellweg, S. (2008). Exposure to manufactured nanostructured particles in an industrial pilot plant. *Annals of Occupational Hygiene*, *52*(8), 695–706.

Estepa, C., & de la Fuente, G. F. (2006). P 200600560.

Fierz, M., Houle, C., Steigmeier, P., & Burtscher, H. (2011). Design, calibration, and field performance of a miniature diffusion size classifier. *Aerosol Science and Technology*, *45*(1), 1–10, http://dx.doi.org/10.1080/02786826.2010.516283.
Fonseca, A.S., Viitanen, A.-K., Koivisto, A.J., Kangas, A., Huhtiniemi, M., & Hussein, T., et al. (2014). Characterization of exposure to carbon nanotubes in an industrial setting. *Annals of Occupational Hygiene*http://dx.doi.org/10.1093/annhyg/meu110.
Gandra, J., Miranda, R., Vilaça, P., Velhinho, A., & Teixeira, J.P. (2011). Functionally graded materials produced by friction stir processing. *Journal of Materials Processing Technology*, *211*(11), 1659–1668, http://dx.doi.org/10.1016/j.jmatprotec.2011.04.016.
Gomes, J., Bordado, J., & Albuquerque, P. (2012). On the assessment of exposure to airborne ultrafine particles in urban environments. *Journal of Toxicology and Environmental Health*, *75*(22–23), 1316–1329.
Gómez, V., Irusta, S., Balas, F., & Santamaria, J. (2013). Intense generation of respirable metal nanoparticles from a low-power soldering unit. *Journal of Hazardous Materials*, *256–257*(0), 84–89, http://dx.doi.org/10.1016/j.jhazmat.2013.03.067.
Gomez, V., Levin, M., Saber, A.T., Irusta, S., Dal Maso, M., Hanoi, R., et al. (2014). Comparison of dust release from epoxy and paint nanocomposites and conventional products during sanding and sawing. [Research Support, Non-U S Gov't]. *Annals of Occupational Hygiene*, *58*(8), 983–994.
Jacobs, C.W.F. (1954). Opacifying crystalline phases present in zirconium-type glazes. *Journal of the American Ceramic Society*, *37*(5), 216–220, http://dx.doi.org/10.1111/j.1151-2916.1954.tb14026.x.
Jervis, T.R., Nastasi, M., Hubbard, K.M., & Hirvonen, J.P. (1993). Excimer laser surface processing of ceramics: process and properties. *Journal of the American Ceramic Society*, *76*(2), 350–355, http://dx.doi.org/10.1111/j.1151-2916.1993.tb03791.x.
Koivisto, A.J., Lyyranen, J., Auvinen, A., Vanhala, E., Hameri, K., & Tuomi, T., et al. (2012). Industrial worker exposure to airborne particles during the packing of pigment and nanoscale titanium dioxide. *Inhalation Toxicology*, *24*(12), 839–849.
Koivisto, A.J., Palomaki, J.E., Viitanen, A.K., Siivola, K.M., Koponen, I.K., & Yu, M., et al. (2014). Range-finding risk assessment of inhalation exposure to nanodiamonds in a laboratory environment. [Research support, Non-U S Gov't]. *International Journal of Environmental Research and Public Health*, *11*(5), 5382–5402.
Kuhlbusch, T.A.J., Quass, U., Koch, M., Fissan, H., Bruckmann, P., & Pfeffer, U. (2004). PM10 source apportionment at three urban back ground sites in the western Ruhr-area, Germany. *Journal of Aerosol Science*, *35*(Supplement 1(0)), 79–90, http://dx.doi.org/10.1016/j.jaerosci.2004.06.027.
Kulmala, M., Vehkamäki, H., Petäjä, T., Dal Maso, M., Lauri, A., & Kerminen, V.M., et al. (2004). Formation and growth rates of ultrafine atmospheric particles: A review of observations. *Journal of Aerosol Science*, *35*(2), 143–176, http://dx.doi.org/10.1016/j.jaerosci.2003.10.003.
Kumar, P., Fennell, P., & Britter, R. (2008). Effect of wind direction and speed on the dispersion of nucleation and accumulation mode particles in an urban street canyon. *Science of the Total Environment*, *402*(1), 82–94, http://dx.doi.org/10.1016/j.scitotenv.2008.04.032.
Lahoz, R., de la Fuente, G.F., Pedra, J.M., & Carda, J.B. (2011). Laser engraving of ceramic tiles. *International Journal of Applied Ceramic Technology*, *8*(5), 1208–1217, http://dx.doi.org/10.1111/j.1744-7402.2010.02566.x.
Minguillon, M.C., Monfort, E., Querol, X., Alastuey, A., Celades, I., & Miro, J.V. (2009). Effect of ceramic industrial particulate emission control on key components of ambient PM10. [Research support, Non-U S Gov't]. *Journal of Environmental Management*, *90*(8), 2558–2567.
Misra, C., Singh, M., Shen, S., Sioutas, C., Hall, P.M., & Sioutas, C., et al. (2002). Development and evaluation of a personal cascade impactor sampler (PCIS). *Journal of Aerosol Science*, *33*, 1027–1047.
Pfefferkorn, F.E., Bello, D., Haddad, G., Park, J.-Y., Powell, M., & McCarthy, J., et al. (2010). Characterization of exposures to airborne nanoscale particles during friction stir welding of aluminum. *Annals of Occupational Hygiene*, *54*(5), 486–503, http://dx.doi.org/10.1093/annhyg/meq037.
Querol, X., Alastuey, A., Rodríguez, S., Plana, F., Ruiz, C.R., & Cots, N., et al. (2001). PM10 and PM2.5 source apportionment in the Barcelona Metropolitan Area, Catalonia, Spain. *Atmospheric Environment*, *35*, 6407–6419.
Querol, X., Viana, M., Alastuey, A., Amato, F., Moreno, T., & Castillo, S., et al. (2007). Source origin of trace elements in PM from regional background, urban and industrial sites of Spain. *Atmospheric Environment*, *41*(34), 7219–7231, http://dx.doi.org/10.1016/j.atmosenv.2007.05.022.
Reche, C., Viana, M., Brines, M., Pérez, N., Beddows, D., Alastuey, A., & Querol, X. (2015). Determinants of aerosol lung-deposited surface area variation in an urban environment. *Science of The Total Environment*, *517*, 38–47.
Romero, M., Rincón, J.M., & Acosta, A. (2003). Crystallisation of a zirconium-based glaze for ceramic tile coatings. *J Eur Ceram Soc*, *23*(10), 1629–1635, http://dx.doi.org/10.1016/S0955-2219(02)00415-6.
Rubahn, H.-G. (1999). *Laser applications in surface science and technology*. John Wiley & Sons: New York.
Sánchez de la Campa, A.M., de la Rosa, J.D., González-Castanedo, Y., Fernández-Camacho, R., Alastuey, A., & Querol, X., et al. (2010). High concentrations of heavy metals in PM from ceramic factories of Southern Spain. *Atmospheric Research*, *96*(4), 633–644, http://dx.doi.org/10.1016/j.atmosres.2010.02.011.
Schmatjko, K. J., Endres, G., Schmidt, U., & Banz, P. H. (1988). Precision machining of ceramic materials by excimer laser irradiation.
Seinfield, J.H., & Pandis, S.N. (2012). *Atmospheric chemistry and physics: From air pollution to climate change*. John Wiley & Sons .
Taylor, J.R., Bull, A.C., & Ceramics, I.O. (1986). *Ceramics glaze technology*. Institute of Ceramics by Pergamon Press .
Toenshoff, H. K., & Gedrat, O. (1991). Absorption behavior of ceramic materials irradiated with excimer lasers.
Van Broekhuizen, P. (2012). Nano matters: building blocks for a precautionary approach [Ph.D. thesis]. Available at: ⟨www.ivam.uva.nl/?nanomatters⟩.
Viana, M., Rivas, I., Querol, X., Alastuey, A., Sunyer, J., & Álvarez-Pedrerol, M., et al. (2014). Indoor/outdoor relationships and mass closure of quasi-ultrafine, accumulation and coarse particles in Barcelona schools. *Atmospheric Chemistry and Physics*, *14*(9), 4459–4472, http://dx.doi.org/10.5194/acp-14-4459-2014.
Voliotis, A., Bezantakos, S., Giamarelou, M., Valenti, M., Kumar, P., & Biskos, G. (2014). Nanoparticle emissions from traditional pottery manufacturing. [Research support, Non-U S Gov't]. *Environmental Science: Processes & Impacts*, *16*(6), 1489–1494.